

**UNIVERSITY OF CRETE
MATERIALS SCIENCE AND TECHNOLOGY
DEPARTMENT**



**Synthesis, Characterization and Study of Photocatalytic
Activity of Organized Mesoporous TiO₂ Frameworks for
Selective Oxidation of Benzyl Alcohols**

Marios Savvakis

Supervisor: Prof. Gerasimos Armatas

HERAKLION 2017

Dedicated to my nieces Barbara and Evangelia

Acknowledgements

First and foremost, I would like to thank my Supervisor and advisor Professor Gerasimos Armatas. It has been an honor to be his Master student. He has taught me how good inorganic chemistry/materials science is done. All his contributions are much appreciated and made my Master experience productive and stimulating. The members of the research group have contributed tremendously with their advices and their outstanding enthusiasm for science. Our group has been a source of friendships and for this reason I would like to thank personally Eirini Koutsouroubi for being the most fun person at the lab, Tzortzina Velegraki for her help on Photoluminescence spectroscopy measurements, Ioannis Tamiolakis, Ioannis Vamvasakis, Ioannis Daskalakis for his help in the synthesis of CMK-3 hard template, Stelios Papadogiorgakis for all the football chats we had and the crucial advices he gave me on catalysis and especially Evangelia (Lia) Skliri for her immense help during my photocatalytic aerobic alcohol oxidation experiments. Without her, this work would not have been the same. My time at University of Crete was made enjoyable due to the many friends that became part of my life. I would like to thank Chara Spanou for her motivation and love during all those years which I will never forget, Cansu Hasan, Ioannis-Ilias Farmakis who since kindergarten has been my brother from another mother, Vasileios Oikonomou for all the fun we had together and for being my partner in "crime", Antonis Papadopoulos for all the football matches we watched together, Alexandros Youlountas, Kanakis Stauroulakis, Odysseas Karavanakis, Mikis Milonakis, Spyros Georgakis, Aris Plexidas and Haris Vlassakis and his wonderful family who treated me like a member of their family. I would also like to thank my pet birds Albus and Belle who made every day at home special with their singing and companionship. Last but not least, I would like to thank my family for all their love and support. My parents Garyfalia Savvaki and Evangelos Savvakis who raised me and supported me my whole life both financially and emotionally in all my pursuits, my sister Grigoria Savvaki who was always there when things turned bad with kind words and compassion, my brother in law Konstantinos Georgoulas to whom and his advices I owe that I have gotten this far and my nieces Barbara and Evangelia Georgoula who make me the happiest man in the world when they smile.

(Page intentionally left blank)

Contents

1. INTRODUCTION

1.1 Porous materials.....	7
1.2 Liquid crystal mechanism (Soft-templating method).....	8
1.3 Hard templating method	8

2. BACKGROUND AND SCOPE OF THE STUDY

2.1 Inorganic chemical semiconductors.....	10
2.2 Titanium dioxide nanostructures	11
2.3 Photocatalytic oxidation of alcohols.....	12

3. EXPERIMENTAL TECHNIQUES AND DETAILS

3.1 Synthesis of mesoporous silica SBA-15.....	13
3.2 Synthesis of mesoporous carbon CMK-3	13
3.3 Preparation of $\text{TiO}(\text{NO}_3)_2$ compound	14
3.4 Synthesis of mesoporous TiO_2	14
3.5 Photocatalytic reactions	15

4. RESULTS AND DISCUSSION

4.1 Thermogravimetric analysis	17
4.2 X-ray diffraction analysis	18
4.3 IR spectroscopy.....	20
4.4 Electron microscopy characterization.....	21
4.5 Nitrogen Porosimetry.....	22
4.6 UV/vis optical and photoluminescence spectroscopy	26
4.7 Photocatalytic study.....	28

5. CONCLUSION.....	35
---------------------------	-----------

6. REFERENCES.....	36
---------------------------	-----------

Περίληψη

Στην παρούσα εργασία πραγματοποιήθηκε η σύνθεση νέων καλά οργανωμένων μεσοπορώδων πλεγμάτων TiO_2 με υψηλή καταλυτική δραστηριότητα. Τα μεσοπορώδη πλέγματα TiO_2 παρασκευάστηκαν με την τεχνική σκληρού εκμαγείου, χρησιμοποιώντας σύμπλοκο $\text{TiO}(\text{NO}_3)_2$ ως πηγή Ti και μεσοπορώδες άνθρακα CMK-3 ως σκληρό εκμαγείο. Πειράματα περίθλασης ακτίνων-X (XRD), ηλεκτρονικής μικροσκοπίας διέλευσης (TEM) και φυσιορόφησης N_2 έδειξαν ότι τα παρασκευασθέντα υλικά διαθέτουν μια καλά οργανωμένη τρισδιάστατη εξαγωνική δομή και παρουσιάζουν υψηλή ειδική επιφάνεια ($256 \text{ m}^2/\text{g}$) και ομοιόμορφο μέγεθος πόρων (μέση διάμετρο πόρου $\sim 7\text{--}8 \text{ nm}$). Επίσης το πορώδες πλέγμα αυτών των υλικών εμφανίζει υψηλή κρυσταλλικότητα και αποτελείται από νανοκρυστάλλους TiO_2 ανατάση. Ο συνδυασμός ενός ημιαγωγικού πλέγματος με μεγάλη εσωτερική επιφάνεια και οργανωμένη πορώδη δομή καθιστά αυτά τα υλικά κατάλληλα για εφαρμογές στη φωτοκατάλυση. Τα αποτελέσματα έδειξαν ότι η προσθήκη αιθυλενοδιαμίνης στη σύνθεση των υλικών έχει ευεργετική δράση στην απόκριση του TiO_2 στην ηλεκτρομαγνητική ακτινοβολία ορατού φωτός. Μολονότι το TiO_2 είναι ένας ημιαγωγός μεγάλου ενεργειακού χάσματος ($E_g = 3.2\text{--}3.4 \text{ eV}$) και απορροφά ακτινοβολία στο υπεριώδες (UV) φάσμα ($\lambda < 380 \text{ nm}$), τα μεσοπορώδη πλέγματα TiO_2 που συνθέσαμε εμφανίζουν εξαιρετική φωτοκαταλυτική δραστηριότητα κάτω από ακτινοβολία UV και ορατού ($\lambda > 420 \text{ nm}$) φωτός. Καταλυτικά πειράματα έδειξαν ότι τα μεσοπορώδη υλικά TiO_2 μπορούν να οξειδώσουν μια σειρά από *para*-υποκατεστημένες βενζυλικές αλκοόλες χρησιμοποιώντας μοριακό O_2 ως οξειδωτικό, δίνοντας υψηλές αποδόσεις ($\sim 86\text{--}100\%$) προς τις αντίστοιχες αλδεΐδες σε σύντομο χρονικό διάστημα (1–2 ώρες). Το μεσοπορώδες πλέγμα TiO_2 επίσης εμφάνισε εξαιρετική σταθερότητα, διατηρώντας την καταλυτική του δράση σε επαναλαμβανόμενους κύκλους κατάλυσης. Τα αποτελέσματα αυτά καθιστούν το παρόν φωτοκαταλυτικό σύστημα $\text{TiO}_2\text{--O}_2$ κατάλληλο για παραγωγή καρβονυλικών ενώσεων από αρωματικές αλκοόλες σε μεγάλη κλίμακα με υψηλές αποδόσεις και υψηλή εκλεκτικότητα.

Abstract

In this study, well-ordered mesoporous TiO₂ frameworks have been successfully prepared by a nano-replication technique, using TiO(NO₃)₂ compound as the Ti source and mesoporous CMK-3 carbon as the hard template. Powder X-ray-diffraction (XRD), transmission electron microscopy (TEM) and N₂ physisorption measurements reveal that the template-free materials possess a three-dimensional (3D) hexagonal mesostructure with large internal BET surface area (up to 256 m²/g) and quite narrow pore-size distribution (~7–8 nm in diameter). Also, the pore walls of these materials exhibit high crystallinity and consist of anatase TiO₂ nanocrystals. The combination of a semiconductive framework with large internal surface area and regular mesoporosity makes these materials highly promising for application in photocatalysis. Our results indicated that incorporation of ethylenediamine in the synthesis of TiO₂ has a beneficial effect on the visible light response of these mesostructures. Although TiO₂ is a wide gap semiconductor that absorbs only UV light ($\lambda < 380$ nm), our mesoporous TiO₂ semiconductors show remarkable UV and visible ($\lambda > 420$ nm) light activity for the photocatalytic oxidation of various *para*-substituted benzyl alcohols in presence of molecular oxygen, giving good-to-high yields (ca. 86–100%) of the corresponding aldehydes within a short reaction time (1 – 2 h). The TiO₂ mesoporous also exert good long-term cycling stability, raising the possibility for the implementation of this TiO₂–O₂ photocatalytic system in large-scale production of carbonyl compounds from aromatic alcohols in high yields and with high selectivity.

Chapter 1: Introduction

1.1 Porous materials

Classically, a *porous matter* is a material that has voids throughout the entire volume of the particles [1]. A translational repetition in 3-D space occurs by the voids, while there is no regularity necessary for a material to be termed “porous”. A material with large gas/solid interface, as the most dominant characteristic, is the most common way to represent a porous solid. Also, it should be noticed that most of them reported in literature are not thermodynamically stable. Porous silica, for example, is just metastable because as soon as the melting point is reached, fusion of primary particles is promoted in the network and it comes to phase separation into a nonporous silica solid. Finally, the thermodynamic stable phase of SiO₂ quartz emerges at very high temperatures. Correspondingly, porous materials can be classified into three categories according to IUPAC rules [2]:

- *Microporous* materials with pore sizes of less than 2 nm.
- *Mesoporous* materials with pore sizes between 2 and 50 nm.
- *Macroporous* materials with pore sizes ranging from 50 nm to several micrometers.

The control over pore size and shape constitutes ordered porous materials to be much more interesting, while their disordered counterparts display high polydispersity in pore geometries. In many cases a material possesses more than one porosity. This could be:

- For *microporous* materials: an additional mesoporosity or macroporosity generated by random grain packing.
- For *mesoporous* materials: an additional macroporosity caused by random grain packing, or an additional microporosity (cracking voids) in the continuous framework.
- For *macroporous* materials: an additional meso- and microporosity, even when the pores are disordered. A material possessing just one type of pore could be more homogenous than one having just a fragment of nicely ordered pore channels.

A good analytical tool for porous materials classification according to the size of their pores is gas sorption analysis. In particular, different characteristics in gas adsorption and desorption isotherms are attributed to pores of different sizes and geometries.

1.2 Liquid crystal mechanism (soft-templating method)

Various chemical methods are used to prepare mesoporous materials. However, the most widespread and efficient method of synthesis is that of liquid-crystal template (LCT). In this method, organized micelles of organic amphiphilic molecules or block copolymers (surfactants) are formed in a polar solution (e.g., water or ethanol). At the surface of the micelles, inorganic matter is then organized and polymerized forming a continuous network. This approach is general and it can be applied to the development of organized materials with dimensions ranging from a few nanometers to a few micrometers.

The mechanism for the formation of these micelles has been extensively investigated in recent years through many studies, but yet remains unclear [3]. Among various suggestions, Beck et al. proposed a liquid-crystalline surfactant model, which seems to describe the development of these materials very well [4]. According to this mechanism, the liquid crystalline phase is formed first which then reacts with the inorganic species (metal oxide-hydroxide monomers or oligomers) in the solution by either electrostatic forces or hydrogen bonding interactions. Then the inorganic components are cross-linked together by a chemical sol-gel process on the surface of micelles to produce organized hybrid inorganic/organic composites. Finally, the surfactant molecules within the pores are removed by ion exchange or high temperature heating to produce a mesoporous material with open-pore structure and large internal surface area. The porous structure of these materials is defined by the structure of the surfactant molecules and exhibits either cubic or hexagonal symmetry.

1.3 Hard templating method

Nanocasting provides an alternative route for the fabrication of mesoporous oxides with controlled composition and textural topology [5]. Originally used for mesoporous carbon (CMK-type materials), this method has been extended to mesoporous metals, such as Pt and Ag, and transition-metal oxides, such as Co_3O_4 , Fe_2O_3 , Cr_2O_3 , CeO_2 and In_2O_3 [6,7,8,9]. This approach involves impregnation and inverse replica solidification of suitable inorganic precursors (usually metal nitrates) within the pore channels of a nanoporous template, such as silica or carbon. After removal of the silica walls, the

shape-reversed templated structure can easily be obtained as a product. In particular, this process involves the following steps:

A) In the *first step* impregnation of the precursor inorganic compounds occurs into the template pores. Specifically, inorganic components can be impregnated by one of the following methods:

i) Two-solvent method: In this method, the dispersion of the mesoporous (hard) template in hexane is mixed with an aqueous solution of metal salts. Generally, the volume of metal precursors should be comparable to the pore volume of the mesoporous material in order to avoid development of microcrystals outside the porous structure of hard template as much as possible. The presence of hexane favors the impregnation and adsorption of the precursor salts inside the template pores.

ii) Solvent evaporation method: This method involves mixing the mesoporous template with metal nitrates in a solution of ethanol. The precursors are expected to be impregnated in the pore system of the template by capillary condensation with slow evaporation of the solvent.

iii) Solid-Liquid method: In this case, the metal salt is mixed with the mesoporous template, forming a homogeneous suspension. Next, the homogeneous mixture is heated until the precursor salt is melt and the impregnation of the precursor compound within the template pores is achieved. Keep in mind that this method is only applicable to precursors whose melting point is lower than their decomposition temperature.

iv) Impregnation-precipitation-calcination method: In this method, metal chlorides are used as precursors, which are impregnated in the mesoporous template. Ammonia is then used in liquid or gaseous phase for the transformation of chlorides into metal hydroxides, and finally calcination takes place in order to form the desired oxide.

B) In the *second step* solidification occurs by heating the precursor compounds inside the template nanopores. Heating may be carried out in an oxidizing or inert atmosphere thus selectively forming the desired oxide phase. This process leads to the formation of a core-shell structure where the metal oxide is the core structure inside the pores (shell).

3) Finally, removal of the template can be achieved via etching with diluted HF (e.g. silica) or high temperature calcination (e.g., carbon template). In this case the mesoporous replicas possess a well-ordered crystalline framework from hexagonal

p6mm ordered nanorods, to cubic *Ia-3d* bicontinuous nanowires, to cubic *Fm-3m* or *Im-3m* interconnected spherical nanocages, derived from mesoporous silicas SBA-15, KIT-5, and FDU-12 or SBA-15 as hard templates, respectively.

An important advantage of this technique is the control of the mesostructure of final product which is achieved by the selection of the desired host material. Although the direct liquid-crystal templating from amphiphilic surfactants has been successfully applied for mesoporous silicates, such as MCM-41 and SBA-15, the synthesis of mesoporous transition-metal oxides is challenging because of the redox instability and phase transition of metal-oxide structures after template removal [10]. Moreover, hard templates have high temperature resistance and could be used for the synthesis of crystalline mesoporous materials which are difficult to obtain with soft-templating technique. However, the hard template method has several drawbacks: The thickness of the lattice in the final material is limited by the diameter of the template pores. For example, in the synthesis of mesoporous metal oxides using SBA-15 as a template, the thickness of the oxide walls must be only 6–10 nm. Finally, this method requires another step, which is the synthesis of the hard template [11].

Chapter 2: Background and Scope of the Study

2.1 Inorganic semiconductors

The electronic structure of semiconductor materials is characterized by an energy interval between the valence band (VB) and conduction band (CB), which each of these have a high density of states. This energy interval is termed bandgap (E_g). Furthermore, for the electron transfer between semiconductor materials and aqueous redox species, it is necessary to determine the highest occupied and lowest unoccupied electronic levels in the semiconductor structure for the reason that those are the energy levels involved in the electron transfer with electrolytes or reactants. All electronic levels in the valence band in most semiconductors are occupied while the levels in the conduction band are empty, as a result the top of the valence band and the highest occupied electronic level coincide. Meanwhile, the bottom of the conduction band in most semiconductors coincides with the lowest unoccupied electronic level. It should be note that the electron affinity (A) is defined as the energy obtained by moving an

electron from the vacuum to the minimum of the conduction band of a semiconductor, while the Fermi level (E_F) defines the chemical potential of electrons in a semiconductor. Primarily, the absolute electronegativity $-\chi$ of a pristine semiconductor is the Fermi level [12].

2.2 Titanium dioxide nanostructures

Titanium dioxide (TiO_2) due to its unique optical and electronic properties is one of the most prominent materials for solar energy applications including photocatalysis. The challenge of high-performance photocatalysts has stimulated significant research efforts into the development of crystalline TiO_2 nanoparticles during the last few years. Although it is a wide gap semiconductor ($E_g = 3.2\text{--}3.4$ eV), TiO_2 is the dominant semiconductor material employed for photocatalytic applications. The excellent photoelectrochemical stability along with its non-toxicity make, for example, TiO_2 suitable for the aerobic photocatalytic organic transformations and degradation of environmental pollutants [13, 14, 15, 16, 17, 18]. In addition, the excellent photocatalytic properties are also the result of the efficient charge carrier separation and higher photon to electron conversion [19].

Mesoporous structures of transition metal oxides with large internal surface area and uniform pores are of immense interest in many technological fields, including catalysis, selective absorption, and separation. These materials can combine complementary functionalities into the inorganic structure such as regular mesoporosity and high catalytic activity. Nanostructured arrays of TiO_2 with ordered mesostructure and high surface area may exhibit unusual properties such as quantum confinement and improved electron transfer kinetics. It is expected that coupling of these functionalities into the same material can provide complementary or enhanced physicochemical characteristics in the former, such as high photocatalytic activity. In addition, nanostructured TiO_2 semiconductors, unlike bulk solids, may offer unique perspectives to sustain photocatalytic chemistry mainly due to the substantial dimensional reduction of the semiconducting framework and the large accessible pore surface. Due to these advantages, the electron-hole recombination could be effectively suppressed in nanoscale semiconductors as a result of the short charge-carrier diffusion length. Therefore, it is reasonable to expect a high photon-to-electron conversion yield in these

systems. Consequently, with the expectation of a highly exposed surface area, a nanostructured array of TiO₂ with a regular pore structure holds more promise for improving the photocatalytic efficiency. This is because a 3D open-pore structure can provide a large number of exposed active sites available for reaction, yet it can enable rapid transport of reactants and products through the catalyst. However, the synthesis of such complex materials is a great challenge because of the low processability of titanium oxo-hydroxide species [TiO_x(OH)_yⁿ⁻] to assemble ordered mesostructures.

2.3 Photocatalytic oxidation of alcohols

Over the last years catalytic oxo-functionalization of organic compounds has received immense attention in the field of organic synthetic chemistry [20]. In this regard, a fascinating possibility is the use of an inorganic semiconductor as the catalyst for the oxidative transformations of organic compounds. Titania appear as a promising catalyst, which is active and selective in various types of photocatalytic oxidation reactions of organic compounds, including alcohols. For the preparation of fragrances and food additives as well as many organic intermediates catalytic transformation of primary alcohols to aldehydes is essential. Great advantages economically and energetically are manifested through the formation of aldehydes (from alcohols) with high yields. On the other hand, molecular oxygen has received much attention as mild oxidant due to its environmental friendly attributes [21]; moreover, it is a superior oxidizing agent for the oxidation of alcohols due to its high reactivity. [22, 23, 24, 25].

In addition, photo-oxidation of 1-phenylethanol yields acetophenone which is a valuable precursor material for the production of many significant organic products, such as resins [26]. The resulting polymeric substances are essential components for the fabrication of various coatings, inks and adhesives. Moreover, acetophenone is an ingredient of fragrances that resemble strawberry, almond and cherry among others [27]. Finally, acetophenone is converted to styrene via a two-step process [28], and it is also used for the synthesis of many pharmaceuticals through the Mannich reaction of dimethylamine with formaldehyde; this process gives β -dimethylamino-propiofenone as the main product [29, 30].

Chapter 3: Experimental Techniques and Details

3.1 Synthesis of mesoporous silica SBA-15

Ordered (TEOS) were added dropwise to the surfactant Pluronic P123 solution, and the resulting mixture was left under stirring for about 24 h at 35 °C. After that, the spherical flask was closed with a glass cap and was left at 100 °C for 24 h under static conditions. The final product was collected by filtration, washed with copious of ethanol and deionized water, and dried at 100 °C for 12 h. In order to remove the template inside the pores, the dry product was heated in an oven at 500 °C for 4 h, using a heating rate of 1 °C/min [31].

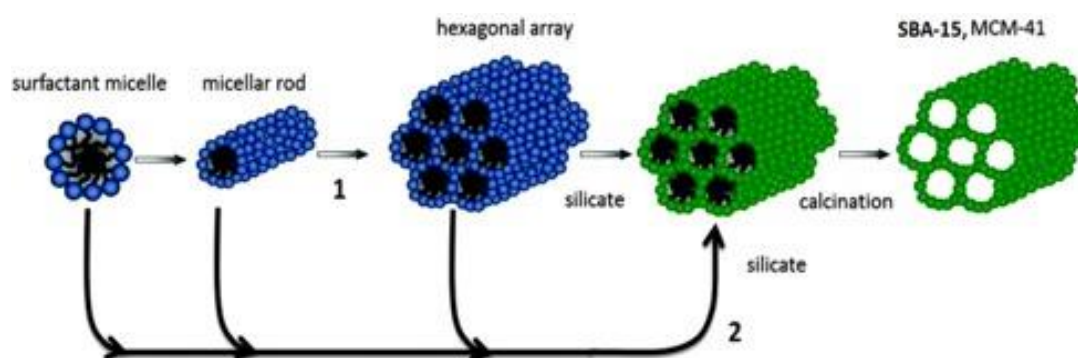


Fig. 1. Synthesis mechanism and structure of mesoporous silica SBA-15.

3.2 Synthesis of mesoporous carbon CMK-3

Briefly, in a spherical flask of 250 mL, 0.28 g of concentrated H_2SO_4 , 2.5 g of sucrose and 2 g of SBA-15 were added in 10 mL of deionized H_2O . The mixture was then stirred moderately for about 24 h. The final product was collected by filtration and was transferred in an over and heated to 100 °C for 6 h, and subsequently to 160 °C for 6 h (1 °C/min heating rate). The sample turned dark brown or black during the thermal treatment in the oven. The silica sample, which contains partially polymerized and carbonized sucrose, was treated again at 100 °C and then at 160 °C using the same heating rate after impregnation of 2/3 of the original reagents, i.e. 0.185 g of H_2SO_4 , 1.65 g of sucrose, and 6.6 mL of deionized H_2O . The as-obtained material was then calcined at 900 °C under vacuum, and the resulting carbon/silica composite sample was

washed with 1M HF solution twice. Finally, the silica-free mesoporous carbon was isolated by filtration, washed with water, and dried at 100 °C for 12 h [32].

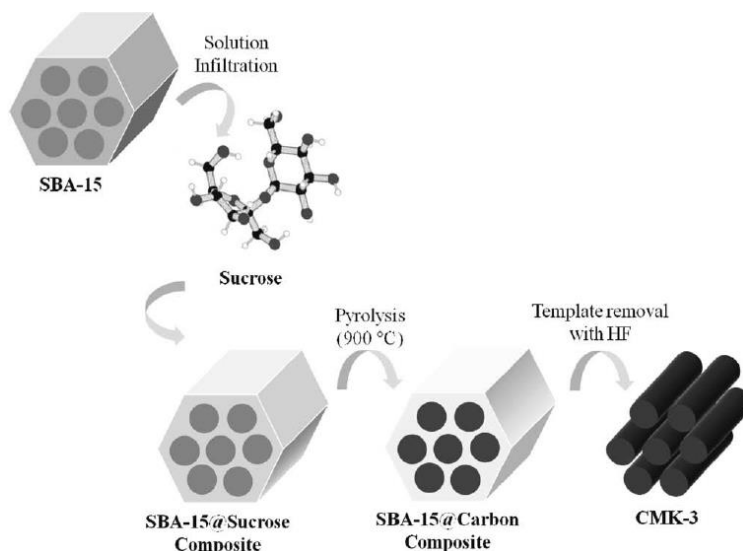


Fig. 2. Synthesis mechanism and structure of mesoporous carbon CMK-3 [33].

3.3 Preparation of $\text{TiO}(\text{NO}_3)_2$ compound

In a typical reaction, 3.5 mL of $\text{Ti}(\text{OC}_3\text{H}_7)_4$ were dissolved in 7 mL ethanol under magnetic stirring. Then, 11 mL of deionized H_2O were added dropwise until a white precipitate was formed. The product $\text{Ti}(\text{OH})_4$ was collected by filtration and dried at 100 °C for 1 h. Next, 1.45 g of $\text{Ti}(\text{OH})_4$ were added to a concentrated HNO_3 solution and the resulting mixture was stirred for about 6 h. The acid solution of $\text{TiO}(\text{NO}_3)_2$ was then kept light protected with aluminum foil in the refrigerator (~5 °C) since it is unstable to higher temperatures and UV light.

3.4 Synthesis of mesoporous TiO_2

In a typical preparation of mesoporous TiO_2 , 0.1 g of CMK-3 was dispersed in 1 mL of anhydrous hexane under stirring at room temperature. In a separate vial, 1 mL (1 mmol/mL) of $\text{TiO}(\text{NO}_3)_2$ solution and 1.5 mL of ethylenediamine (*en*) were

mixed to form a clear solution. This solution was added dropwise to the CMK-3 suspension, and the resulting mixture was kept under stirring at 80 °C until complete evaporation of the solvents (typically within ~1–2 days). Consequently, the as-obtained dry product was thermal annealing at 200 °C for 2 h under vacuum to undergo crystallization of TiO₂. Finally, the carbon template was completely removed by calcination in air at 550 °C for 3 h, using a heating rate of 1 °C/min. Different hexagonally ordered mesoporous TiO₂ materials (denoted as TiO₂*_en*_T, where *en* indicates presence of ethylenediamine in the reaction mixture and T is the calcination temperature) with high crystallinity and accessible pore channels were prepared by the nano-replication technique, using different amounts of reactants as shown in Table 1. For comparative studies, bulk-like TiO₂ solid was also prepared according to the above procedure but without using a hard template.

Table 1. Synthesis of mesoporous TiO₂ materials using different reaction conditions.

Samples	CMK-3 (g)	Hexane (mL)	TiO(NO₃)₂ (1mmol/mL)	C₂H₄(NH₂)₂ (mL)	Heating Temperature
TiO ₂ <i>_en</i> _550	0.1	1	1 mL	1.5	550 °C
TiO ₂ <i>_en</i> _600 ^[a]	0.1	1	1 mL	1.5	600 °C
TiO ₂ _550	0.1	1	1 mL	-	550 °C
Untemplated TiO ₂	-	-	1 mL	1.5	550 °C

[a] For TiO₂*_en*_600 sample crystallization was achieved by heating in N₂ atmosphere at 600 °C for 1 h.

3.5 Photocatalytic reactions

The photocatalytic oxidations of aryl alcohols were carried out as follows: a mixture of alcohol (0.1 mmol) and catalyst (25 mg) in oxygen-bubbled (ca. 20 ml min⁻¹) acetonitrile (3 mL, HPLC-grade) was placed in a 4-mL glass reactor closed with a Teflon cap (Fig.3). The mixture was irradiated with a Variac Cermax 300 W Xenon lamp ($\lambda > 360$ nm) as the light source. Before switching on the lamp, the catalytic grains were kept in suspension by vigorous magnetic stirring for 30 min. During irradiation, the reaction mixtures were cooled with water bath (ca. 20 °C) and monitored by gas chromatography (GC). The reaction conversion and the products characterization was performed on a Shimadzu GCMS-QP2010 Ultra chromatograph by withdrawing small

aliquots from the reaction mixture. Primary benzyl alcohols **1–6** were commercially available of high purity (>99.8%) and used as received (Sigma-Aldrich).

For recycling experiments, the photocatalyst was recovered by centrifugation, dried under vacuum, and used for the next catalytic run.

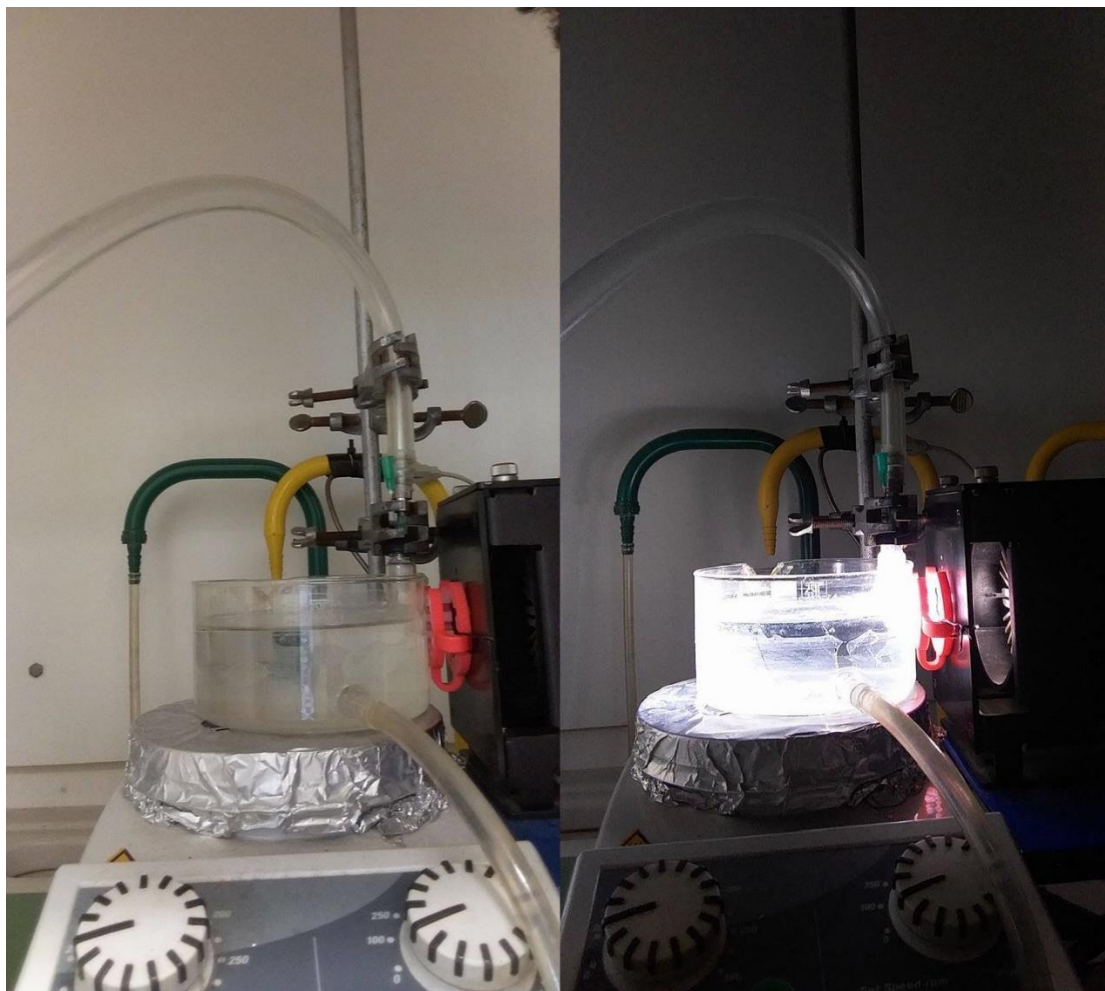


Fig. 3. Photocatalytic setup for photo-oxidation experiments.

Chapter 4: Results and Discussion

4.1 Thermogravimetric analysis

Thermogravimetric analysis (TGA) was carried out for the carbon/TiO₂ composite material in order to determine the optimal temperature for obtaining the mesoporous TiO₂ materials. TGA was performed using a Perkin-Elmer Diamond system. Thermal analysis was conducted from 40 to 600 °C in an air flow of ~150 mL/min with a heating rate of 10 °C/min.

In Fig. 4, the TGA profile of the carbon/TiO₂ composite shows a weight loss of 10% in the temperature range of 40–120 °C, which is attributed to the liberation of physisorbed water and organic solvents. The continuous weight loss (ca. 30%) in the 440–600 °C temperature range is attributed to the removal by oxidation of the carbon CMK-3 template. Based on these results, we have chosen the 550 °C as the calcination temperature for our composite materials in order to completely remove the carbon template. The efficient removal of the template was also confirmed by elemental C, H and N analysis, which showed that only trace amount of carbon (ca. 0.23%) are present in the mesoporous products. Elemental C, H and N analysis was performed on a Perkin-Elmer 2400 Series II CHNS/O instrument.

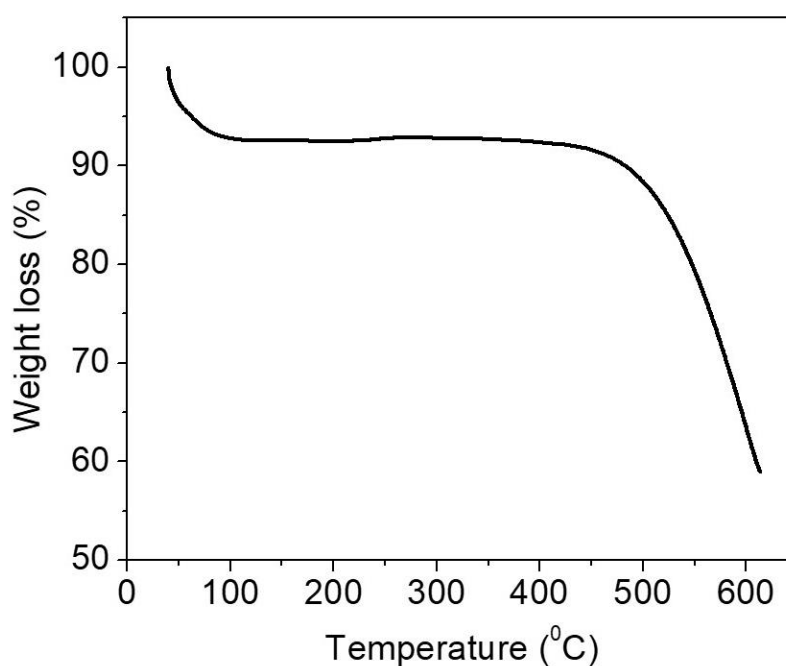


Fig. 4. TGA profile for carbon/TiO₂ composite material.

4.2 X-ray diffraction analysis

The crystallinity and phase purity of the mesoporous materials were characterized by X-ray diffraction (XRD). XRD patterns were collected on a PANalytical X'pert Pro MPD X-ray diffractometer using Cu K α radiation ($\lambda = 1.540598 \text{ \AA}$) in Bragg–Brentano geometry.

Fig. 5 displays the low-angle XRD pattern of mesoporous SBA-15 silica, where three well-resolved diffraction peaks can be readily seen. The indexing of the Bragg diffractions is consisted with a hexagonal $p6mm$ unit cell with lattice parameter $a_0=10.8 \text{ nm}$.

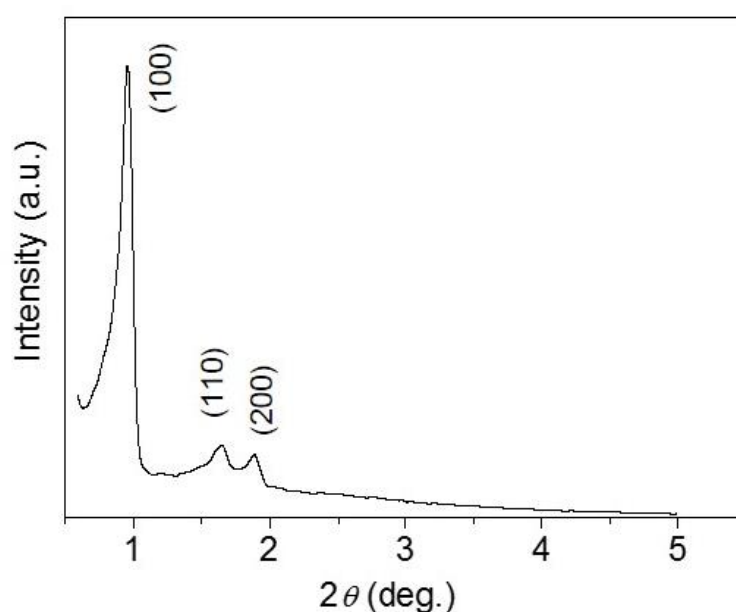


Fig. 5. Low-angle XRD pattern of mesoporous SBA-15 silica.

The wide-angle XRD patterns of the mesoporous TiO₂ samples in Fig. 6 showed several broad Bragg diffraction peaks, suggesting nanocrystalline TiO₂. All the diffractions can be readily assigned to the anatase phase of TiO₂ with a hexagonal lattice structure (space group: $p6mm$). It is worth noting that no other diffraction peaks were detected corresponding to impure crystalline phases, such as brookite or rutile TiO₂. Moreover, the well-defined diffraction peaks in the XRD patterns suggests the high crystallinity of the samples. On the basis of the Scherrer analysis of the (101) reflection [$d_p = 0.9\lambda/B \cos\theta$, where λ is the source wavelength and B is the full-width half-maximum of the diffraction peak centered at 2θ degrees, assuming spherical-shaped

particles], the average domain size of the TiO₂ crystallites was estimated to approximately 7–8 nm for the mesoporous materials (see Table 2).

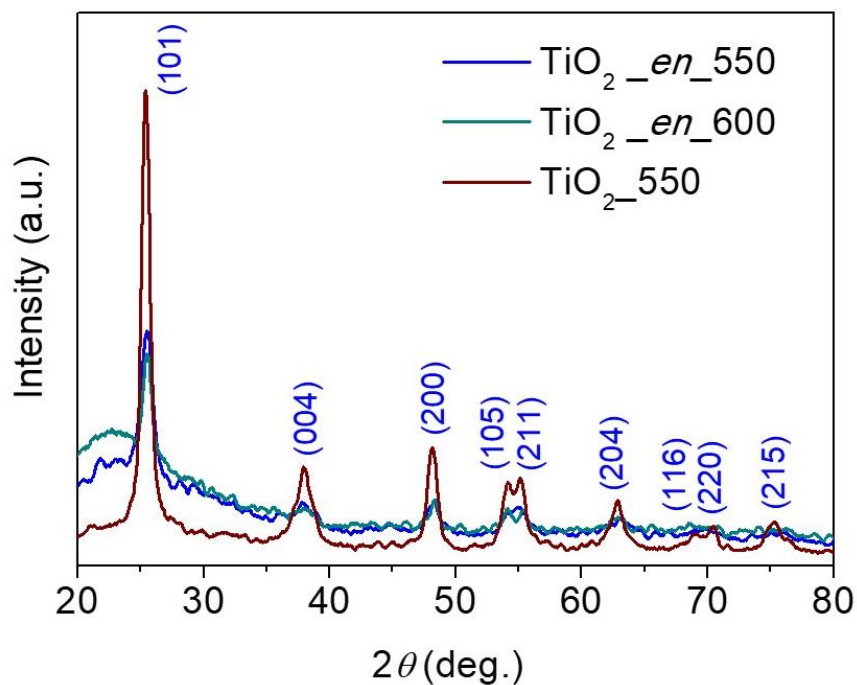


Fig. 6. X-ray diffraction patterns of the mesoporous TiO₂_en_550, TiO₂_en_600 and TiO₂_550 materials.

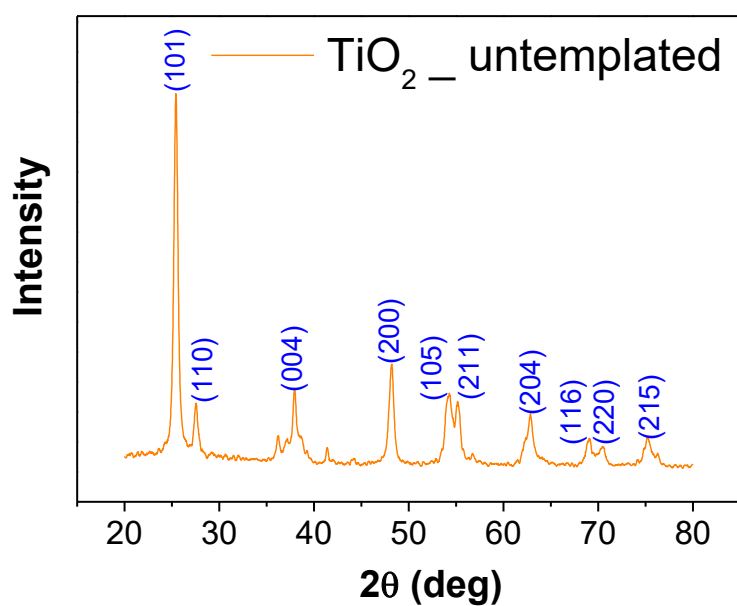


Fig. 7. X-ray diffraction pattern of the untemplated TiO₂ sample.

4.3 IR spectroscopy

The molecular structure of TiO₂ frameworks was characterized by infrared (FT-IR) spectroscopy. FT-IR spectra were recorded on a Perkin Elmer Model Frontier FT-IR spectrometer with 2 cm⁻¹ resolution. Samples were prepared as KBr pellets.

Fig. 8 displays the FT-IR spectra of mesoporous TiO₂_{en}_550 and TiO₂_550 materials. The absorption peaks at 462 cm⁻¹ and 797 cm⁻¹ can be assigned to the vibration bands of the O–Ti–O bonds in anatase structure [34, 35]. While the peaks at 1627 cm⁻¹ and 3388 cm⁻¹ are attributed to the vibration modes of absorbed H₂O molecules and surface hydroxyl groups, respectively [35].

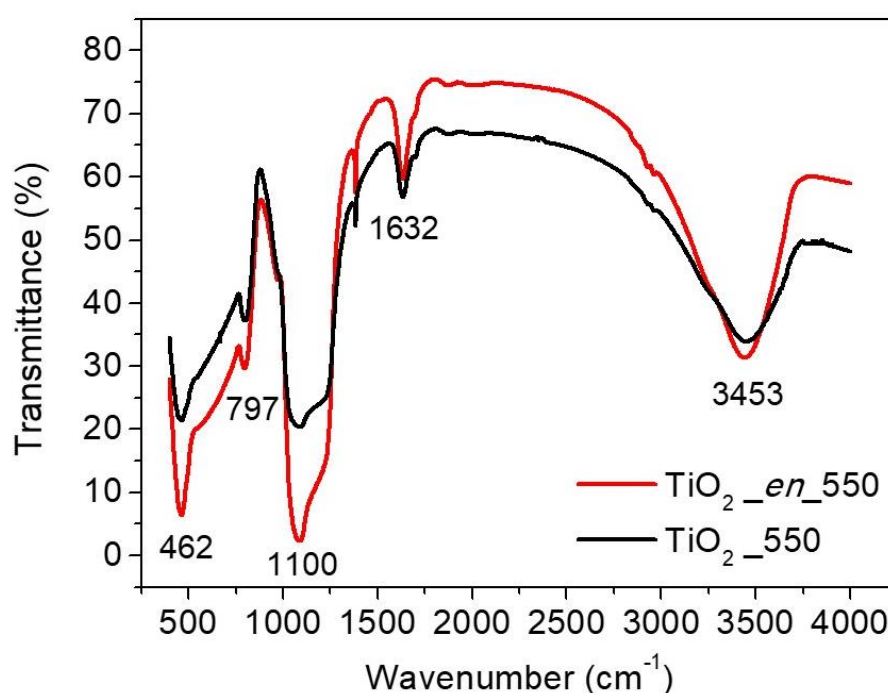


Fig. 8. FT-IR spectra of the mesoporous TiO₂_{en}_550 and TiO₂_550 materials.

4.4 Electron microscopy characterization

To verify the mesoscopic order of the as-prepared TiO_2 materials, we utilized transmission electron microscopy (TEM). TEM images were taken with a JEOL JEM-2100 electron microscope (LaB₆ filament) operating at an accelerated voltage of 200 kV. Samples were prepared by dispersing fine powders in ethanol using sonication, followed by depositing a drop of solution onto the carbon-coated Cu grid and evaporating the solvent in air.

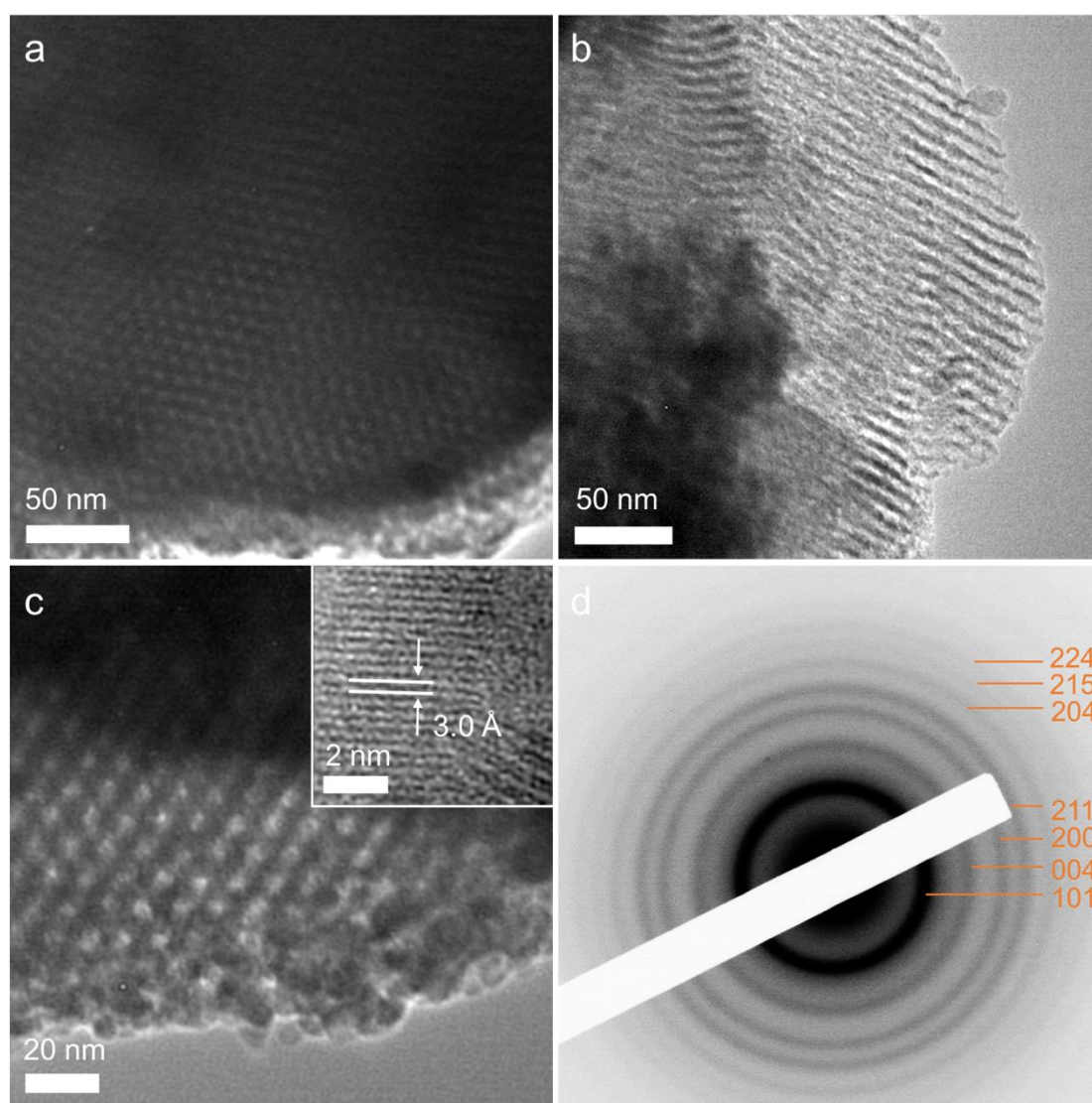


Fig. 9. (a-c) Typical TEM images and (d) SEAD pattern for mesoporous TiO_2 _en_550 catalyst. Inset of panel c: HRTEM image showing the lattice fringes of anatase structure.

The TEM images confirm that the replicas preserve the crystal structure of the carbon template. Fig. 9 shows typical TEM images of mesoporous TiO₂_en_550, revealing well-defined long-range hexagonal arrays of uniform mesopores. Analysis of the TEM images indicates an average framework wall thickness of ~4 nm and a pore diameter of ~6–7 nm. The framework wall thickness of TiO₂_en_550 is approximately commensurate with the pore diameter of the parent carbon template (~3.6 nm, see Fig. 11). To probe the crystal structure of the mesoporous framework, we utilized high-resolution TEM (HRTEM) and selected-area electron diffraction (SAED). The HRTEM image (Fig. 9c, inset) displays a portion of the porous framework and demonstrates the high crystallinity of the TiO₂. It shows distinct lattice fringes with 3.5 Å interplanar spacing, which correspond to the (101) crystal planes of anatase TiO₂. Furthermore, the SAED pattern in Fig. 9d reveals that TiO₂ nanocrystals embedded in the pore walls are randomly oriented, showing a series of Debye-Scherrer diffraction rings that can be assigned to the anatase structure of TiO₂ (JCPDS card No. 21-1272). This indicates that the pore walls are obviously crystalline, as suggested by wide-angle XRD patterns.

4.4 Nitrogen porosimetry

The mesoporosity of the template-free materials was determined by nitrogen physisorption measurements. The N₂ adsorption and desorption isotherms were measured at –196 °C with a Quantachrome Nova 3200e volumetric analyzer. Before analysis, the samples were degassed at 150 °C under vacuum (<10⁻⁴ mbar) for 12 h in order to remove moisture from the material's surface. The surface areas were calculated using the Brunauer-Emmett-Teller (BET) model on the adsorption data for 0.05 – 0.25 relative pressure (P/P₀) region [36], the total pore volumes were calculated from the adsorbed amount at the P/P₀ of 0.99, and the distributions of pore sizes were derived from the adsorption branch of isotherms, using the non-local density functional theory (NLDFT) method for cylindrical pore geometry [37].

Figs. 10 and 11 show the N₂ adsorption-desorption and the corresponding pore-size distribution plots for mesoporous SBA-15 silica and CMK-3 carbon templates. Analysis of the adsorption data with the BET method gives a surface area of 650 m²/g and a total pore volume of 0.88 cm³/g for the mesoporous silica. Given an estimation

of the mesopore diameter (D_p) at 7.6 nm and the unit cell size (a_o) at 10.8 nm (see Fig. 4), the pore wall thickness (WT) is about 3.2 nm, according to the equation $WT=a_o-D_p$. Similarly, analysis of the adsorption data of mesoporous carbon indicates a surface area of $632 \text{ m}^2/\text{g}$ and a total pore volume of $0.73 \text{ cm}^3/\text{g}$. Given an estimation of the mesopore diameter (D_p) at 3.4 nm and the unit cell size (a_o) at 10 nm, the pore wall thickness (WT) was found to be $\sim 6.6 \text{ nm}$, according to the equation $WT=a_o-D_p$.

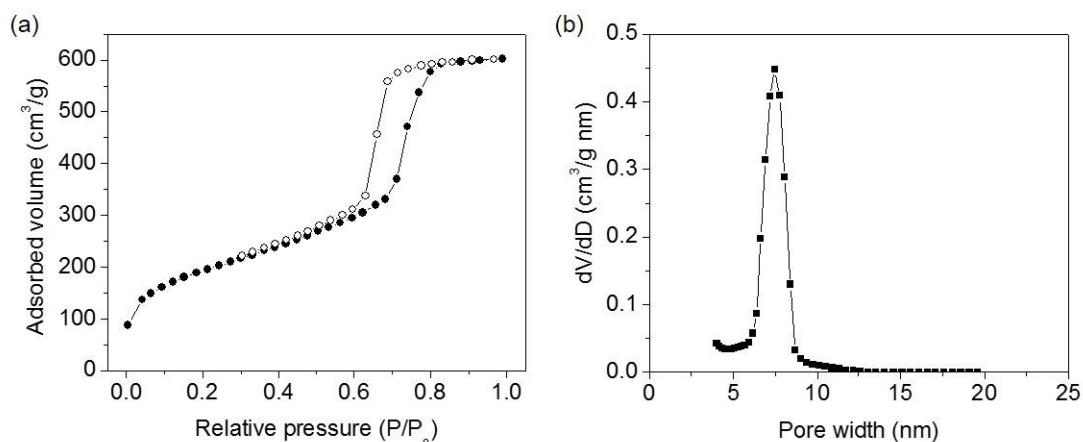


Fig. 10. (a) Nitrogen adsorption and desorption isotherms at 77 K and (b) the corresponding NLDFT pore size distribution for mesoporous SBA-15 silica, indicating a mesopore size of 7.6 nm.

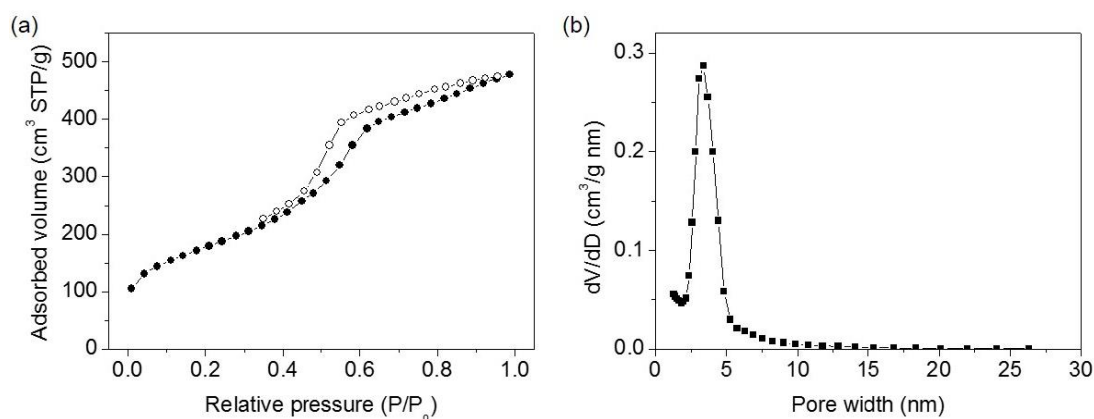


Fig. 11. (a) Nitrogen adsorption and desorption isotherms at 77 K and (b) the corresponding NLDFT pore size distribution for mesoporous CMK-3 carbon, indicating a mesopore size of 3.4 nm.

Fig. 12 shows N_2 adsorption-desorption and the corresponding pore-size distribution plots for mesoporous TiO_2 materials along with those of non-templated analogues. The

adsorption isotherms of mesoporous samples are of type IV with a combination of H₂- and H₃-type hysteresis loop according to IUPAC classification, which is ascribed to an interconnected mesoporous structure with cylindrical pores. The mesoporous TiO_{2_en_550} and TiO_{2_en_600} samples show a peculiar double hysteresis loop which is related to the capillary condensation and evaporation of nitrogen in mesoporous domains with different pore size. The BET surface areas and total pore volumes of mesoporous TiO₂ assessed from the adsorption branch of the isotherms are 124–256 m²/g and 0.23–0.38 cm³/g, respectively. It can be observed that the surface area and pore volume of mesoporous TiO₂ decreases with increasing the calcination temperature (600 °C), probably due to the partial shrinkage of the titanium oxide mesostructure during the solidification process. The mesoporous TiO₂ materials feature a narrow NLDFT pore-size distribution with the peak at approximately 7–8 nm (Fig. 12, insets), which coincides well with the TEM results. This pore size is related to the pores left after decomposition of the carbon template (~6.6 nm in pore wall thickness). Combining with XRD and TEM data, these results suggest that the mesoscale structure of TiO₂ is a good positive replica of the pristine silica (SBA-15) template (pore size ~ 7.6, wall thickness ~ 3.2 nm, see Fig. 10), used for the carbon replication.

Table 2. Textural properties of mesoporous TiO_{2_en_550}, TiO_{2_en_600} and TiO_{2_550} replicas casted from CMK-3 mesostructure ($a_0 = 10$ nm) and untemplated TiO₂ sample.

Sample	specific surface area (m ² /g)	Pore Volume ^[a] (cm ³ /g)	Pore width (nm)	Crystallite size (nm)
TiO _{2_en_550}	240	0.38	7.1	6.0
TiO _{2_en_600}	124	0.23	7.1	6.7
TiO _{2_550}	256	0.37	8.7	7.8
Untemplated TiO ₂	38	0.07	-	-

[a] Total pore volume at P/P₀ = 0.98.

Crucially, the hard-templated process yielded a framework structure of TiO₂ composition with mesoscale porosity. For comparison, in the absence of template, the Ti oxo-hydroxo species are assembled into bulk-like microparticles. This is demonstrated by the N₂ adsorption-desorption isotherms shown in Fig. 12d, the shape

of which confirms the difference in morphology between the templated and non-templated TiO₂ materials. The N₂ adsorption-desorption isotherms of the untemplated TiO₂ are of type II without hysteresis loop, typically found with random microporous networks with slit-like pores. Analysis of the adsorption data reveals that this material has a BET surface area of 38 m²/g and a total pore volume of 0.07 cm³/g, which are very low compared to those of the templated materials. All textural parameters of the mesoporous TiO₂ and untemplated sample are given in Table 2.

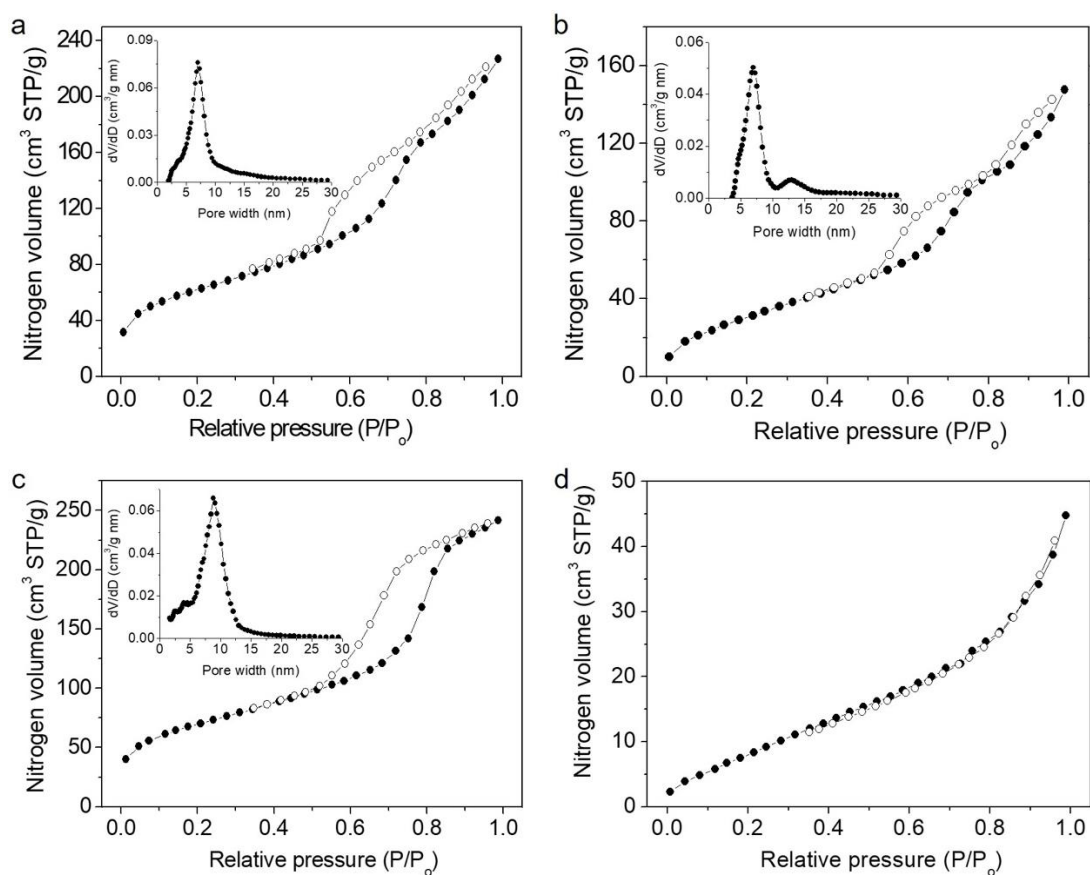


Fig. 12. N₂ adsorption and desorption isotherms at -196 °C and the corresponding NLDFT pore-size distribution plots (insets) of the mesoporous (a) TiO₂_{en_550}, (b) TiO₂_{en_600} and (c) TiO₂₅₅₀ materials and (d) untemplated TiO₂ sample.

4.6 UV/vis optical and photoluminescence spectroscopy

The electronic structure of as-prepared TiO₂ materials was characterized by diffuse reflectance ultraviolet-visible/near-IR (UV-vis/NIR) spectroscopy. Diffuse reflectance UV-vis/near-IR spectra were obtained on a Perkin Elmer Lambda 950 optical spectrophotometer in the wavelength range 200–1200 nm. BaSO₄ powder was used as a 100% reflectance standard and base material on which the powder sample was coated. Diffuse reflectance data were converted to absorption using the Kubelka-Munk function $\alpha/S = (1-R)^2/(2R)$, where R is the measured reflectance and α , S are the absorption and scattering coefficients, respectively. The band gaps of the samples were estimated from the onset of absorption data converted from reflectance [38].

As shown in Fig. 13, all the mesoporous TiO₂ materials display an intense optical absorption onset in the UV/near-visible region (380 nm), which is associated with an energy gap transition at 3.3–3.4 eV. This energy gap is slightly wider than the band gap absorption of the bulk TiO₂ solid (~3.2 eV), possible due to the nanosize wall thickness of the TiO₂ framework.

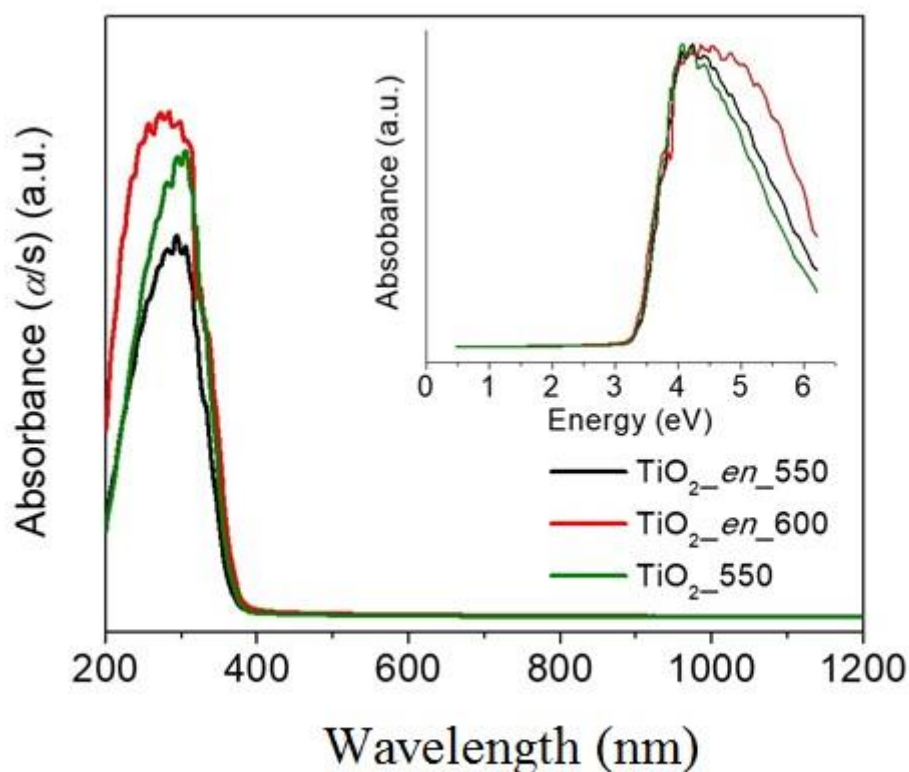


Fig. 13. Solid-state UV-vis/NIR spectra for mesoporous TiO_{2_en_550}, TiO_{2_en_600} and TiO_{2_550} materials.

The electronic band structure of the mesoporous TiO₂ materials was also investigated with photoluminescence (PL) spectroscopy. Fig. 14 shows PL emission spectra recorded for the mesoporous TiO₂_{en_550} and TiO₂₅₅₀ catalysts under excitation with 330 nm light. Both samples showed an intense PL emission at ~400 nm (3.10 eV) which is related to the band-to-band optical transition. In addition, strong PL signals were seen at the ~482 nm (2.57 eV) and ~500 nm (2.48 eV) region that related to shallow (defect levels) and deep intergap states, respectively, in TiO₂. This suggests that shallow localized electronic states exist near the conduction band edge and oxygen vacancies of TiO₂, which may act as electron hole traps. Electron transitions from the defect states (oxygen vacancies) to the top of the valence band are presumably responsible for photon emission with low energy in oxygen-deficient TiO₂ [39].

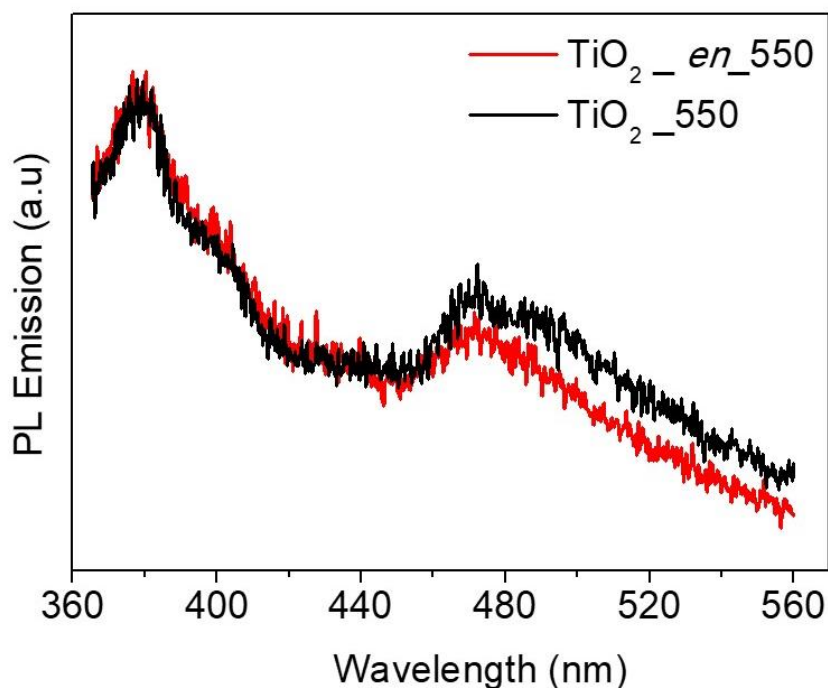


Fig. 14. PL spectra for mesoporous TiO₂_{en_550} and TiO₂₅₅₀ materials.

4.7 Photocatalytic study

Photo-oxidation of 1-phenylethanol

To assess the photocatalytic activity of the mesoporous TiO₂ materials and to determine the optimum reaction conditions, the UV-visible light irradiated oxidation of 1-phenylethanol (**1**) using different catalysts and loadings was initially studied. The photocatalytic reactions were performed using the same conditions, i.e. 0.1 mmol **1**, 25 mg catalyst, 3 mL acetonitrile (CH₃CN) and O₂ bubbling (20 mL/min). As can be seen from Fig. 15a and Table 3, all the mesoporous TiO₂ materials exhibit a very good and competitive photocatalytic performance, with TiO₂_{en_550} being the most active catalyst. The TiO₂_{en_550} mesoporous achieves a ~88% conversion of **1** to acetophenone (**1a**) within 2 h of irradiation. Notably, the mesoporous TiO₂_{en_550} showed higher activity than the untemplated TiO₂ sample. In particular, if untemplated TiO₂ was introduced as the catalyst, it afforded a conversion of **1** of ~76% in 2 h under identical conditions. This might be attributed to the lower surface area of untemplated sample, which results in a decreased number of surface active sites available for catalysis. In agreement to this assumption, the low activity of the TiO₂_{en_600} could be attributed to the lower internal surface area compared to the TiO₂_{en_550}. Moreover, the presence of ethylenediamine in the synthesis of TiO₂ may induce the formation of midgap states in the band structure of TiO₂, which are responsible for the visible light absorption of TiO₂. Evidence for this was obtained from the visible-light irradiated oxidation of **1** over mesoporous TiO₂_{en_550}. Although, TiO₂ is a wide gap semiconductor that absorbs only UV light ($\lambda < 380$ nm), TiO₂_{en_550} catalyst exhibits a small (~29%) but detectable conversion to **1a** under $\lambda > 420$ nm light illumination (see Table 3). In consistency with the visible light response of TiO₂_{en_550}, elemental C, H and N analysis on this sample showed a N concentration of about 0.1 atom%, implying the presence of N 2p states above the TiO₂ valence band maximum. Such localized midgap p states can narrow the band gap of the semiconductor, inducing visible light responsive activity. Overall, these findings suggest that the high photocatalytic activity of the TiO₂_{en_550} can be attributed to the small grain size of the TiO₂ nanocrystals and the 3D ordered mesoporous structure, which facilitates reactant contact with the TiO₂ surface, and the presence of midgap electronic states within the band gap of TiO₂, which induce visible light absorption and possible electron-hole separation. Meanwhile, controlled experiments showed that in the absence

of catalyst or UV-visible light irradiation, no oxidation of **1** occurred (over a 2 h reaction period), indicating that the oxidation reaction is indeed a photocatalytic process.

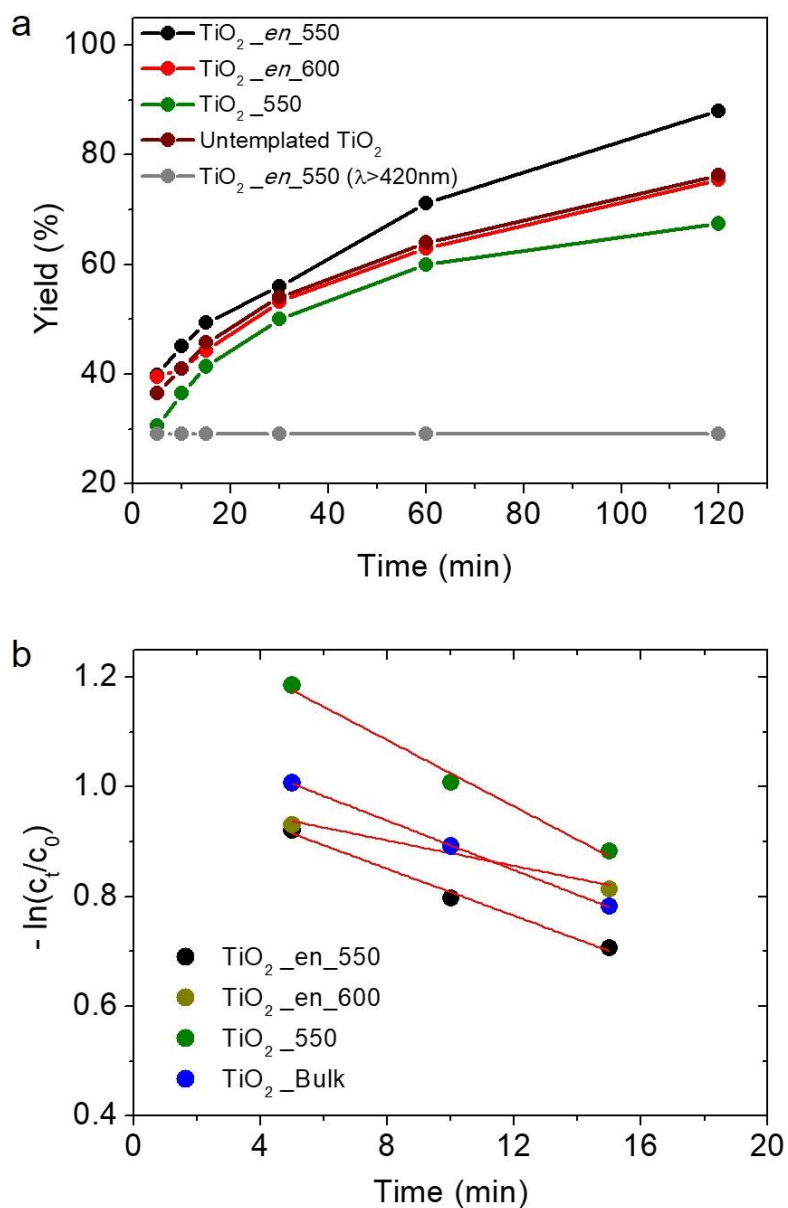


Fig. 15. (a) Time courses and (b) pseudo first-order rate plots (C_0 , C_t are the initial and final (at time t) concentrations of 1-phenylethanol, respectively) for the photo-oxidation of 1-phenylethanol (**1**) catalyzed by mesoporous TiO₂_en_550, TiO₂_en_600 and TiO₂_550 catalysts, and untemplated TiO₂ sample. In panel b: The corresponding red lines are fit to the data.

Assuming that the oxygen concentration remains constant during the reaction, the photo-oxidation process can be considered as pseudo-first order reaction:

$$\ln(1 - x) = -kt \quad (1)$$

where, k is the rate constant and x is the conversion of **1** alcohol at irradiation time t .

The kinetics plots of the conversion of **1** versus the time are shown in Fig. 15b and the corresponding k values for **1** photo-oxidations are listed in Table 3.

Table 3. Conversion yield and reaction rate constant (k) for photo-oxidation of 1-phenylethanol (**1**) to acetophenone (**1a**) over various TiO₂-based catalysts.^[a]

Catalyst	Conversion yield ^[b] (%)	Rate constant, k (min ⁻¹)
TiO ₂ _en_550	88	0.021
TiO ₂ _en_600	76	0.012
TiO ₂ _550	68	0.030
Untemplated TiO ₂	76	0.020
TiO ₂ _en_550 ^[c]	29	-

[a] Reaction conditions: 0.1 mmol **1**, 25 mg catalyst, 3 mL CH₃CN, O₂ flow (ca. 25 mL/min), 2 h, 20 °C, UV-visible light ($\lambda > 360$ nm) irradiation. [b] Based on the consumption of **1** determined by GC-MS analysis (conversion = $100 \times (C_o - C_t) / C_o$, where C_o , C_t are the initial and final (after time t) concentration of the product at a certain time t of the photocatalytic reaction). [c] This experiment was performed under visible light ($\lambda > 420$ nm) irradiation.

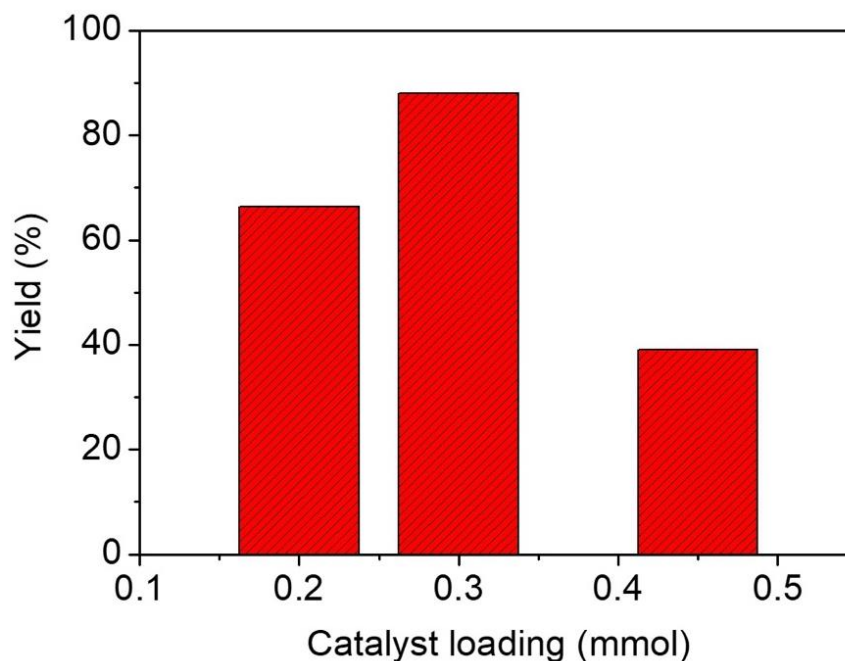


Fig. 16. Photocatalytic oxidation of **1** under varying concentrations of catalyst. Reaction conditions: 0.1 mmol **1**, TiO₂*_en_550* catalyst, 3 mL CH₃CN, O₂ flow (ca. 25 mL/min), 2 h, 20 °C, UV-visible light ($\lambda > 360$ nm) irradiation.

The photocatalytic reaction also strongly depends on the catalyst loading. We found that the optimum catalyst loading for photo-oxidation of **1** was attained at ~8 mg/mL (0.3 mmol), see Fig. 16. The TiO₂ concentration-dependent oxidation rate of **1** can be explained by the enhancement of the light absorption by the catalyst's particles. However, as illustrated in Fig. 16, excess amount of catalyst (more than 12 mg/mL) may counter this effect, leading to a decrease in **1** oxidation efficiency, presumably due to the light scattering effect from the particle surface.

The TiO₂*_en_550* catalyst also demonstrated very good stability under the examined conditions. The reusability of the catalysts was assessed by performing three repeated catalytic tests, in which **1** was oxidized under the reaction conditions described above. After each test, the catalyst was recovered from the reaction mixture by filtration, washed several times with deionized water and used for the next catalytic run. The photocatalysis results, shown in Fig. 17, indicated that the conversion level of **1** remains as high as 84–88% (after 2 h irradiation time) after three catalytic runs, reflecting the excellent reusability of the catalyst.

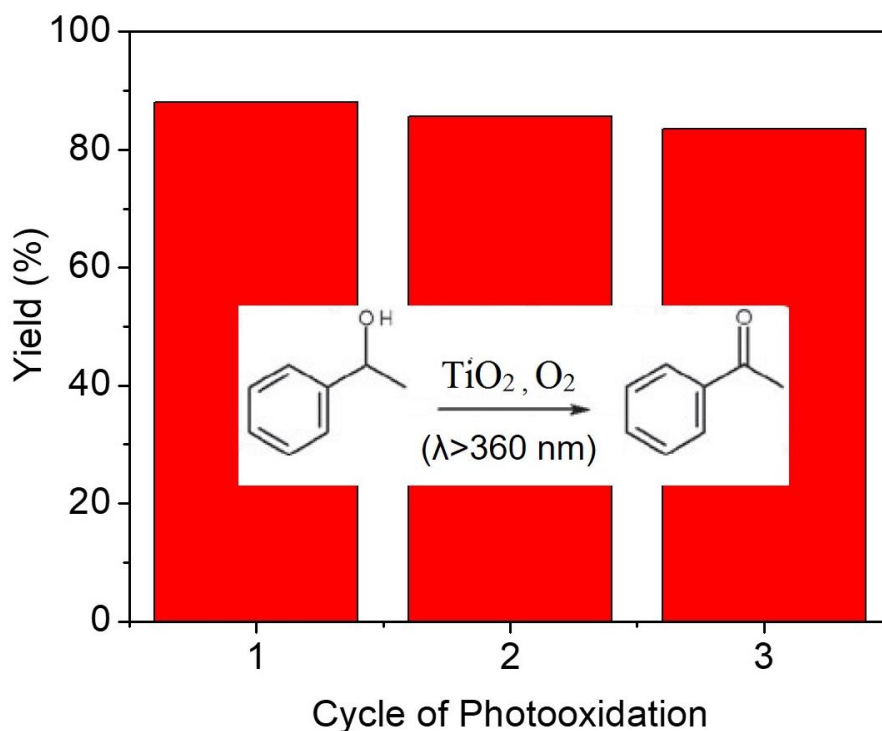


Fig. 17. Recycling study of the mesoporous TiO₂_en_550 catalyst.

Photo-oxidation of various para-substituted benzyl alcohols

To study the general applicability of the above photo-oxidation process, various *para*-substituted benzyl alcohols were examined. As can be seen in Fig. 18a and Table 4, all substituted benzyl alcohols were oxidized to the corresponding aryl aldehydes in good-to-excellent isolated yields (86–100%) within only 2 h irradiation, as identified by GC–MS. All the catalytic reactions were performed under similar conditions using TiO₂_en_550 catalyst and oxygen as oxidant. The 4-methoxy- (**2**), 4-methyl- (**3**) and 4-chloro- (**4**) substituted benzyl alcohols were selectively oxidized by TiO₂_en_550, giving the corresponding aldehydes (**2a**, **3a** and **4a**) in 100% conversion yield. However, the oxidation of electron-deficient 4-nitro benzyl alcohol (**5**) and benzyl alcohol (**6**) substrates proceeded slower than the electron-rich alcohols **2** and **3**, giving the corresponding aldehydes in 86 and 95%, respectively, in 2 h. This is attributed to the electron-withdrawing ability of the *para*-substituted nitro and hydrogen groups of **5** and **6** alcohols, respectively. Notably, in all photo-oxidation reactions the chemoselectivity to the corresponding aldehydes is nearly 100%, and indeed side reactions to oxidized fragments or even CO₂ production are negligible.

Beside the product evolution study, a formal kinetic analysis for the oxidation of various *para*-substituted benzyl alcohols was also performed. Assuming that the reactions can be considered as pseudo-first order with respect to the benzyl alcohol (see Fig. 18b), the reaction rate constants (k) were determined according to Eq. (1) and the results are summarized in Table 4. It appears that the kinetic activity of **2–6** benzyl alcohols is remarkably affected by the nature of the *para*-substituent group, in which the photo-oxidation reaction proceeds faster as the electron-donating ability of the substituent group increases. For example, photo-oxidation of **2** (MeO-substituted) proceeds faster than the corresponding oxidation of benzyl alcohols **6** (H-substituted) and **3** (Me-substituted), as inferred by the relative rate constant ratio of $k_{\text{MeO}}/k_{\text{H}} = 3.4$ and $k_{\text{MeO}}/k_{\text{Me}} = 1.6$, respectively. Substrates that contain electron-acceptor groups such as chloro- (**4**) and nitro- (**5**) benzyl alcohols were also converted to the corresponding aldehydes, but in slower reaction rates. These results indicate that a positive charge or a radical cation intermediate could be formed in the transition state of the rate-determining step, which is better stabilized by the electron donating substitute. Such a radical cation has been suggested to be active intermediate in side-chain oxidation reactions of aromatic alcohols proceeded via an electron transfer (ET) mechanism [40]. Overall, these findings suggest that the TiO₂_{en}-550–O₂ photocatalytic system represents an expeditious approach towards the laboratory and large-scale production of carbonyl compounds from aromatic alcohols in high yields and with high selectivity.

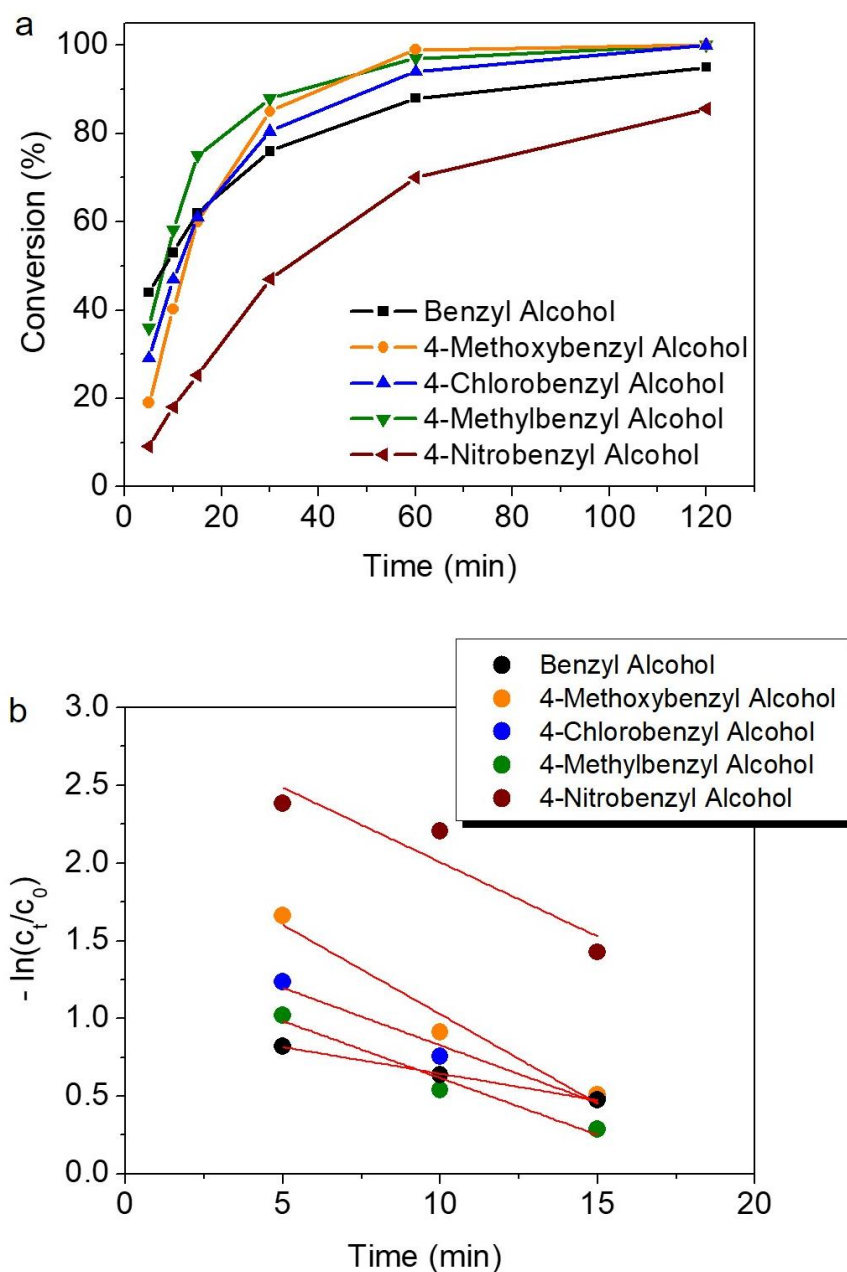
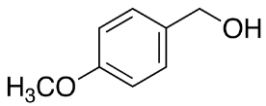
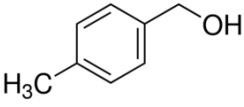
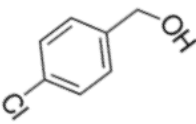
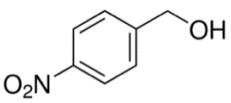
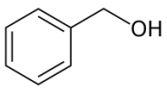


Fig. 18. (a) Time courses and (b) pseudo first-order rate plots (C_0 , C_t are the initial and final (at time t) concentrations of alcohol, respectively) for the photo-oxidation of various *para*-substituted benzyl alcohols catalyzed by mesoporous TiO₂_{en}_550 catalyst. In panel b: The corresponding red lines are fit to the data.

Table 4. Conversion yield and reaction rate constant (k) for photo-oxidation of various *para*-substituted benzyl alcohols over mesoporous TiO₂_en_550 catalyst.

Substrate	Conversion yield ^[a] (%)	Rate constant, k (min ⁻¹)
 4-methoxybenzyl alcohol (2)	100	0.115
 4-methylbenzyl alcohol (3)	100	0.073
 4-chlorobenzyl alcohol (4)	100	0.074
 4-nitrobenzyl alcohol (5)	86	0.095
 Benzyl alcohol (6)	95	0.034

[a] Based on the consumption of alcohol determined by GC-MS analysis (conversion = $100 \times (C_0 - C_t) / C_0$, where C_0 , C_t are the initial and final (after time t) concentration of the product at a certain time t of the photocatalytic reaction).

Chapter 5: Conclusion

In conclusion, well-ordered mesoporous TiO₂ frameworks have been successfully prepared by nano-replication technique, using TiO(NO₃)₂ compound as a Ti source and mesoporous CMK-3 as a hard template. These materials possess a three-dimensional hexagonal mesostructure and exhibit open-pore structure with large internal surface area (up to 256 m²/g) and narrow pore-size distribution (~7–8 nm in diameter) according to the X-ray diffraction, high-resolution TEM, electron diffraction and N₂ physisorption measurements. Moreover, the pore walls of these materials are highly crystalline and consist of anatase TiO₂. The synthesis of a visible-light responsive TiO₂ photocatalyst is significantly affected by the experimental conditions, in which the ethylenediamine used here introduces midgap electronic states between the band gap structure of TiO₂. As a result, although TiO₂ is a wide gap semiconductor that absorbs only UV light ($\lambda < 380$ nm), our TiO₂*_en_550* catalyst exhibit remarkably visible light photo-oxidation activity.

The hexagonal mesoporous TiO₂ frameworks demonstrated great application perspectives in UV and visible light driven oxidation of *para*-substituted aryl alcohols in the presence of molecular oxygen as oxidant. The high chemical yields to the corresponding aryl aldehydes and the absences of oxidative products and CO₂ make the present catalytic system synthetically useful.

References

- [1] J. Rouquerol, *Recommendations for the Characterization of Porous Solids, Pure & Applied Chemistry*. **67** 1994, 1739.
- [2] K.S.W. Sing, D.H. Everett, R.A.W. Haul, L. Moscou, R.A. Pierotti, J. Rouquerol, T. Siemieniewska, *Pure & Appl. Chem.* **57** 1985, 603.
- [3] M. Janicke, D. Kumar, G. D. Stucky, B. F. Chmelka, *Stud. Surf. Sci. Catal.* 1994, **84**, 243.
- [4] J.S. Beck, J.C. Vartuli, W.J. Roth, *J. Am. Chem. Soc.* 1992, **114**, 10834.
- [5] A. H. Lu, F. Schuth, *Adv. Mater.*, 2006, **18**, 1793.
- [6] Y. Sakamoto, T. Ohsuna, K. Hiraga, O. Terasaki, C. H. Ko, H. J. Shin, R. Ryoo, *R. Angew. Chem., Int. Ed.* 2000, **39**, 3107.
- [7] Tian, B. Z. Liu, X., Solovyov, L. Liu, Z. Yang., H. Zhang, Z. Xie, S. Zhang, F. Tu, B. Yu, C. Terasaki, O. Zhao, *D. J. Am. Chem. Soc.* 2004, **126**, 865.
- [8] Tian, B. Z. Liu, X. Y. Yang, H. F. Xie, S. H. Yu, C. Z. Tu, B. Zhao, D. Y. *Adv. Mater.* 2003, **15**, 1370.
- [9] Laha, S. Ryoo, R. *Chem. Commun.* 2003, **17**, 2138.
- [10] G. Soler-Illia, G.J.A. Sanchez, C. Lebeau, B. Patarin, *J. Chem. Rev.* 2002, **102**, 4093.
- [11] L. Pan, H. Qiu, C. Dou, Y. Li, L. Pu, J. Xu, Y. Shi, *Int. J. Mol. Sci.* 2010, **11**, 2636.
- [12] K. Rajeshwar, *Fundamentals of Semiconductor Electrochemistry and Photoelectrochemistry*, Arlington Texas, University of Texas at Arlington, 2007.
- [13] M. Zhang, C. Chen, W. Ma, J. Zhao, *Angew. Chem. Int. Ed.* **47** 2008, 9730.
- [14] G. Palmisano, V. Augugliaro, M. Pagliaro, L. Palmisano, *Chem. Commun.* 2007, **33**, 3425.
- [15] C.C. Chen, W.H. Ma, J.C. Zhao, *Chem. Soc. Rev.* 2010, **39**, 4206.
- [16] A.L. Linsebigler, G.Q. Lu, J.T. Yates, *Chem. Rev.* 1995, **95**, 735.
- [17] M.R. Hoffmann, S.T. Martin, W. Choi, D.W. Bahnemann, *Chem. Rev.* 1995, **95**, 69.
- [18] S. Yurdakal, G. Palmisano, V. Loddo, V. Augugliaro, L. Palmisano, *J. Am. Chem. Soc.* 2008, **130**, 1568.
- [19] X. Chen, S. S. Mao, *Chem. Rev.* 2007, **107**, 2891.

-
- [20] S.R.A. Sheldon, J.K. Kochi, *Metal-Catalyzed Oxidations of Organic Compounds*, Academic Press, New York, NY, 1981.
- [21] S.R.A. Sheldon, W.C. Arends, A. Dijksman, *Catal. Today* 2000, **57**, 157.
- [22] C. Li, Q. Zhang, Y. Wang, H. Wan, *Catal Lett.*, 2008, **120**, 126
- [23] U. R. Pillai, E. Sahle-Demessie, *Green Chem.* 2004, **6**, 161
- [24] M. S. Kwon, N. Kim, C. M. Park, J. S. Lee, K.Y. Kang, J. Park, *Org Lett.*, 2005, **7**, 1077
- [25] H. Siegel, M. Eggersdorfer. "Ketones" Ullmann's Encyclopedia of Industrial chemistry, Weinheim, Wiley-VCH, 2002.
- [26] G. A Burdock, *Flavor Ingredients 6th edition*, New York, CRC Press, 2010.
- [27] S. Wilen, H. Kremer, B. Chester, I. Waltcher *Chem. Educ.* 1961, **38**, 304.
- [28] S. Marshall, *Pharmaceutical Manufacturing Encyclopedia 3rd edition*. New York, William Andrew Publishing, 2007.
- [29] G. Kumar, T. Braish. *Process Chemistry in the Pharmaceutical Industry*, New York, CRC Press, 2007.
- [30] S. Maxwell, Charles E. *Organic Syntheses*. New York, Wiley 1943.
- [31] D. Zhao, Q. Huo, J. Feng, B.F. Chmelka, G.D. Stucky, *J. Am. Chem. Soc.* 1998, **120**, 6024.
- [32] S. Jun, S. Joo, R. Ryoo, M. Kruk, M. Jaroniec, Z. Lui, T. Ohsuna, and O. Terasaki *J. Am. Chem. Soc.* 2000, **122**, 10712.
- [33] S. Bernard, P. Miele *J. Ceram. Sci. Tech*, 2013, **4**, 113.
- [34] G. Soler-Illia, A. Louis, and C. Sanchez, *Chemistry of Materials*, 2002, **14**, 750.
- [35] J. C. Yu, L. Z. Zhang, Z. Zheng, and J. C. Zhao, *Chemistry of Materials*, 2003, **15**, 2280
- [36] S. Brunauer, L. S. Deming, W. E. Deming, *J. Am. Chem. Soc.*, 1940, **62**, 1723.
- [37] P.I. Ravikovitch, D. Wei, W.T. Chueh, G.L. Haller, A.V. Neimark, *J. Phys. Chem. B*, 1997, **101**, 3671.
- [38] W. W. Wendlandt, H. G. Helcht, New York, Wiley Interscience, 1966, **21**.
- [39] J. Shi, J. Chen, Z. Feng, T. Chen, Y. Lian, X. Wang, C. Li *J. Phys. Chem. C* 2007, **111**, 693.
- [40] E. Baciocchi, M. Bietti, O. Lanzalunga, *Acc. Chem. Rev.* 2000, **33**, 243.